




Superparamagnetic MoS₂@Fe₃O₄ nanoflowers for rapid resonance-Raman scattering biodetection

Ting Zhang¹, Xueying Chu^{1,*} , Fangjun Jin¹, Mingze Xu¹, Yingjiao Zhai¹, and Jinhua Li^{1,*}

¹Ministry of Education Key Laboratory for Cross-Scale Micro and Nano Manufacturing, Nanophotonics and Biophotonics Key Laboratory of Jilin Province, Changchun University of Science and Technology, 130022 Changchun, People's Republic of China

Received: 28 December 2021

Accepted: 24 May 2022

Published online:
19 June 2022

© The Author(s), under exclusive licence to Springer Science+Business Media, LLC, part of Springer Nature 2022

ABSTRACT

Sensors for rapid and reliable detection of biomolecules are crucial for clinical medical diagnoses. Here, a rapid, ultra-sensitive, magnetic-assisted biosensor based on resonance Raman scattering at MoS₂@Fe₃O₄ composite nanoflowers is presented. Raman shifts and X-ray photoelectron spectra indicated that the composite was formed via Fe–S covalent bonds. Convenient magnetic separations could be performed because of the superparamagnetic Fe₃O₄ nanoparticles. MoS₂ E_{2g}¹ and A_{1g} Raman peaks were used as probe signals for anti-interference immunoassays. The probe unit of the immunoassay also included goat anti-human IgG molecules that were used as the target analyte. Au substrates coupled with the goat anti-human IgG were used as capture units to form sandwich biosensors. Because of the magnetic enrichment, the detection limit was improved by three orders-of-magnitude and the detection time was reduced from 1.5 h to 1 min. Sandwich biosensors using MoS₂@Fe₃O₄ nanoflowers as Raman probes could be very promising sensors for proteins, antigens, and other immunogenic biopolymers, as well as for corpuscular viruses and cells.

1 Introduction

Rapid and accurate biological detection of pathogenic biological materials has been particularly important since the outbreak of COVID-19. Challenges facing most detection methods are complex, time-consuming procedures, and low target concentrations [1]. Biological Raman detection is attractive because of its fingerprint characteristics, narrow half-widths, non-interference from water, and no photobleaching [2].

These offer the possibility of accurate and simple low-concentration bioassays [3]. With regard to shortening detection times, superparamagnetic nanoparticles (NPs) benefit from sensitive responses to external magnetic fields, no coercivity, and no remanence. Superparamagnetic Fe₃O₄ NPs are biocompatible and can be used in clinical medicine. Its high saturation magnetization enables rapid magnetic enrichment and separations [4, 5]. Fe₃O₄ NPs can be accurately accumulated at required sites by

Address correspondence to E-mail: xueying_chu@cust.edu.cn; lijh@cust.edu.cn

applying an external magnetic field for rapid enrichment of target molecules. Thus, they improve the detection limit and shorten the detection time [6–8].

Magnetic-Raman dual-functional bioassays have demonstrated improved detection limits for miRNA [9], antigens [10], and malachite green isothiocyanate [11]. Moreover, Fe₃O₄ superparamagnetic nanoparticles have significantly shortened detection times [12], and magnetic separations are more convenient. Previous studies were mainly focused on composites of superparamagnetic nanoparticles and noble metal nanostructures for magnetically assisted surface-enhanced Raman scattering [13, 14].

In contrast to surface-enhanced Raman scattering, resonance Raman scattering (RRS) from inorganic nanomaterials does not require the assistance of metallic nanostructures. The target signals also do not require organic Raman reporters or contrast enhancers, which simplifies the procedure [15–17]. Previous reports have used RRS signals from semiconductors (ZnO and ZnS) for femto-molar-level immunological detection [18]. Unlike those for zinc-based semiconductors, the MoS₂ bandgap is in the visible light region. Thus, MoS₂ RRS can be excited with a 532-nm laser source, instead of the ultraviolet light required for ZnO or ZnS. This makes detection safer, less costly, and no autofluorescence interference has been observed from bulk MoS₂ [19–21]. Therefore, RRS of MoS₂ is promising for biosensing. However, the complexation of Fe₃O₄ and MoS₂ for RRS-based biological detection has not been reported.

MoS₂@Fe₃O₄ nanocomposites were fabricated, and the E_{12g}¹ and A_{1g} vibrational modes of MoS₂ were used as RRS probe signals for immunoassays. The magnetic separation and enrichment improved the detection limit and shortened the detection time. This magnetic-assisted rapid RRS detection strategy was simple, low cost, environmentally safe, and could be used for early detection of various pathogens, infectious diseases, and cancers.

2 Experimental section

2.1 Materials

Iron chloride hexahydrate (FeCl₃·6H₂O, 99.0%), iron sulfate heptahydrate (FeSO₄·7H₂O, 99.0%), ammonium molybdate tetrahydrate (H₂₄Mo₇N₆O₂₄·4H₂O,

99.9%), N-(3-dimethylaminopropyl)-N-ethylcarbodiimide hydrochloride (EDC), and thiourea (CH₄N₂S, 99%) were purchased from Aladdin (Shanghai, China). Sodium hydroxide (NaOH, Analytical Reagent) was obtained from Sinopharm Chemical Reagent Co. Ltd. Albumin Bovine V (BSA) was obtained from Beijing Genthold. N-Hydroxysuccinimide (NHS) was purchased from Sigma-Aldrich. Phosphate buffer solution (PBS) was purchased from Meilunbio (Dalian, China). Human IgG and goat anti-human IgG were purchased from Beijing Dingguo Changsheng Biotechnology Co. Ltd. Deionized water (18.2 MΩ·cm) was used throughout.

2.2 Characterization

X-ray diffraction (XRD) patterns were acquired with a Rigaku D/MAX using Cu-Kα radiation (Rigaku Corporation, Japan). The sample morphologies were imaged with scanning electron microscopy (SEM, Quanta FEG-250, FEI Co. Ltd., USA) and transmission electron microscopy (TEM, TecnaiG220S-Twin, USA). X-ray photoelectron spectra (XPS) were acquired with a Thermo Escalate 250Xi XPS spectrometer (Thermo Scientific, USA). RR spectra were acquired with a confocal Raman spectrometer (Horiba Lab Ram HR evolution, Japan). Vibrating sample magnetometry measurements were performed with a 736-VSM Controller (Ohio, USA).

2.3 Synthesis of MoS₂@Fe₃O₄ nanocomposites

MoS₂@Fe₃O₄ nanocomposites were prepared via coprecipitation and hydrothermal methods. Fe₃O₄ NPs were prepared via coprecipitation with a slight modification [22]. Fe²⁺ and Fe³⁺ ions were precipitated with 2-mol/L NaOH until the pH reached 10, and were then mechanically stirred for 30 min under N₂. The Fe₃O₄ NP product was magnetically separated and rinsed with ultrapure water until the supernatant was neutral.

To fabricate MoS₂@Fe₃O₄ nanocomposites, (NH₄)₆Mo₇O₂₄·4H₂O and CH₄N₂S were dissolved in 15 ml of deionized (DI) water in the mass ratio 1:2.2 and sonicated for 15 min. Then, 500 μl of the Fe₃O₄ NP solution (0.15 mg/ml) was added and the mixture was further sonicated for 30 min, placed into a Teflon container, and kept at 200 °C for 8 h. After allowing it to cool to room temperature, the reaction

product was magnetically separated and cleaned with DI water and absolute ethanol, in sequence. The preparation of pure MoS₂ was the same, except for the addition Fe₃O₄ NPs in the hydrothermal process.

2.4 Sandwich Raman immunoassay protocol

The synthesis and working principle of the sandwich biosensor are illustrated in Scheme 1. The biosensor was composed of three parts: a Raman probe signal unit (part A), a Au substrate capture unit (part B), and the immunoassay (part C).

For the preparation of the Raman probe signal unit in part A, a 200- μ l solution of MoS₂@Fe₃O₄ composites (0.007 mg/ml) was mixed with the same volume of goat anti-human IgG (660 nM), followed by shaking at 37 °C for 1.5 h. Then, the resulting MoS₂@Fe₃O₄-antibody complex was magnetically enriched and washed twice to remove excess antibodies. Then, 200 μ l (0.2 mg/ml) of BSA in a PBS solution was added and the mixture shaken at 37 °C for 1.5 h to block unreacted active sites. Finally, the MoS₂@Fe₃O₄-antibody Raman probe was washed with DI water and then magnetically separated and captured.

The Au substrate capture unit was prepared as described previously[18]. As depicted in part B of Scheme 1, human IgG was used as the target analyte

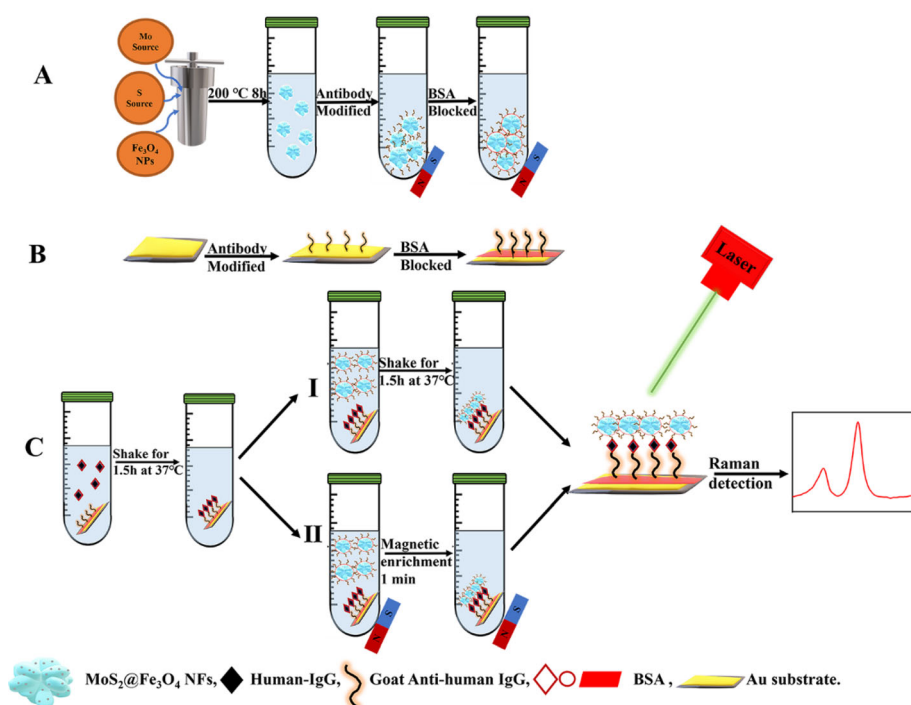
in the immunoassay. In part C of Scheme 1, the goat anti-human-IgG-capture Au substrate was immersed in a human IgG analyte solution with various concentrations. After shaking at 37 °C for 1.5 h, the substrate with the captured analyte was rinsed. Here, two strategies were used to study the effects of the external magnetic field on the immunoassay results. In strategy I, the substrate with the captured analyte was immersed in the solution containing the MoS₂@Fe₃O₄ Raman probe and gently shaken for various periods of time (6 min, 1 h, or 1.5 h) at 37 °C. In strategy II, the substrate was also immersed in the Raman probe solution, but was then placed under an external magnetic field (1.2 T) for several minutes (6 min, 3 min, 1 min, or 0.5 min) instead of being shaken.

3 Results and discussion

3.1 Characteristics of the MoS₂@Fe₃O₄ composites

XRD was performed to determine the crystal structure of the composites (see Fig. 1). The patterns for pure MoS₂ and Fe₃O₄ NPs were also acquired for comparison. The diffraction peaks at $2\theta = 29.5^\circ, 34.8^\circ, 42.4^\circ, 52.9^\circ, 56.5^\circ,$ and 62.1° corresponded to the (220),

Scheme 1 Schematic of Raman probe signal unit (A), Au substrate capture unit (B), and immunoassay process (C)



(311), (400), (422), (511), and (440) planes of Fe_3O_4 crystals (PDF#72-2303) [23]. The peaks at $2\theta = 13.2^\circ$, 32.5° , 38.8° , and 58.0° corresponded to the (002), (100), (103), and (110) planes of MoS_2 crystals (PDF#37-1492). For the composites, diffraction peaks from both MoS_2 and Fe_3O_4 were observed. Because the composites were magnetically separated and carefully washed, the XRD patterns indicated that the Fe_3O_4 NPs were combined with MoS_2 . No unknown peaks appeared, indicating negligible impurities in the $\text{MoS}_2@\text{Fe}_3\text{O}_4$ composites.

The scanning electron microscope image in Fig. 2a indicated that the $\text{MoS}_2@\text{Fe}_3\text{O}_4$ composites were 300–900-nm flower-like nanostructures. Magnetic NPs on the petals of MoS_2 NFs were marked in the transmission electron microscope image in Fig. 2b. For comparison, scanning electron and transmission electron microscopy images of MoS_2 flowers are also shown in Fig. 2c, d and no granular particles were observed.

XPS of $\text{MoS}_2@\text{Fe}_3\text{O}_4$ NFs and pure Fe_3O_4 nanoparticles are plotted in Fig. 3. As shown in Fig. 3a, the Fe 2p spectrum via peak fitting had Fe(II)-O (710.2 eV, 724.4 eV) and Fe(III)-O (712.4 eV, 725.6 eV) peaks [24, 25]. In the composite with MoS_2 , the Fe 2p spectra (Fig. 3b) also indicated divalent and trivalent states. The peaks at 726.4 eV (Fe $2p_{1/2}$) and 713.2 eV (Fe $2p_{3/2}$) were attributed to Fe(III)-O bonds, and the peaks at 724.1 eV (Fe $2p_{1/2}$) and 711.2 eV (Fe

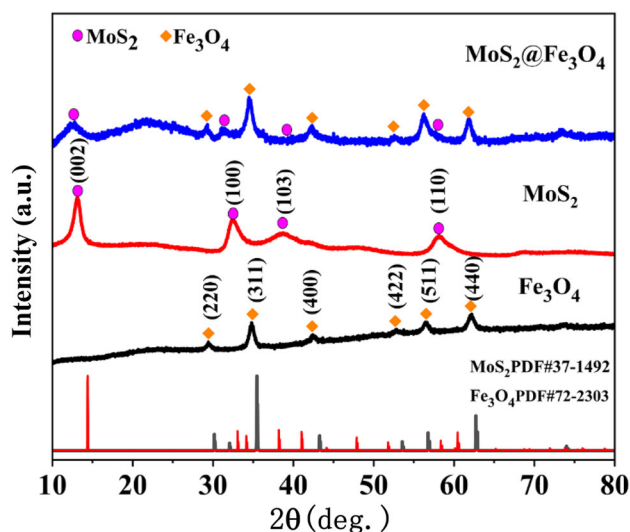


Fig. 1 X-ray diffraction patterns for Fe_3O_4 NPs, MoS_2 , and $\text{MoS}_2@\text{Fe}_3\text{O}_4$ composites. Standard PDF cards are noted

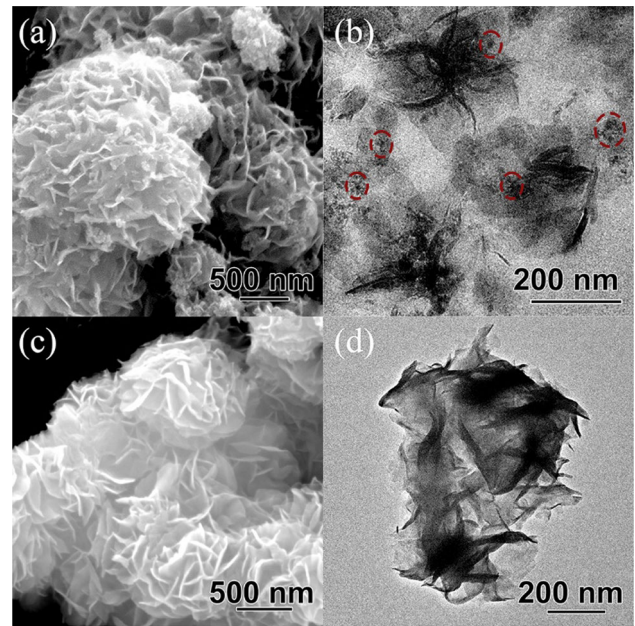


Fig. 2 a Scanning electron microscope (SEM) image and b transmission electron microscope (TEM) image of $\text{MoS}_2@\text{Fe}_3\text{O}_4$ nanoflowers (NFs). c SEM image and d TEM image of MoS_2 NFs

$2p_{3/2}$) were in agreement with Fe(II)-O bonds [26]. In addition, Fe-S bonds were observed at 710.3 eV [Fe (III)-S] and 708.4 eV [Fe (II)-S] [27], which indicated that the composites were formed with covalent bonds. The peaks at 718.5 eV and 732.5 eV were assigned to Fe (III) and Fe (II) satellites, respectively [28]. The peaks at 530.3 eV and 531.7 eV in the O1s spectra (Fig. 3c) were attributed to Fe-O and O-H in Fe_3O_4 , respectively. The peaks at 530.9 eV in the O1s spectrum (Fig. 3d) corresponded to Mo-O, which may be attributed to oxidization during the synthesis [29, 30]. The characteristic peaks at 228.6 eV and 231.8 eV in the spectra of Mo 3d (Fig. 3e) were attributed to Mo $3d_{5/2}$ and Mo $3d_{3/2}$, respectively. The component at 225.7 eV corresponded to S 2s in the Mo-S bond [31], and the peak at 235.6 eV corresponded to Mo (VI) [32, 33]. In Fig. 3f, the S $2p_{1/2}$ and S $2p_{3/2}$ peaks were located at 162.7 eV and 161.5 eV, respectively, in the composite spectra, which were similar to other reported data or MoS_2 [34].

Characteristic vibrational fingerprints were reflected in the RRS. As noted above, the 1.29–1.9-eV bandgap of MoS_2 enabled resonant 532-nm laser excitation. In Fig. 4a, the Raman peaks at 379.0 cm^{-1} and 405.1 cm^{-1} were attributed to the in-plane $\text{E}_1 2g$

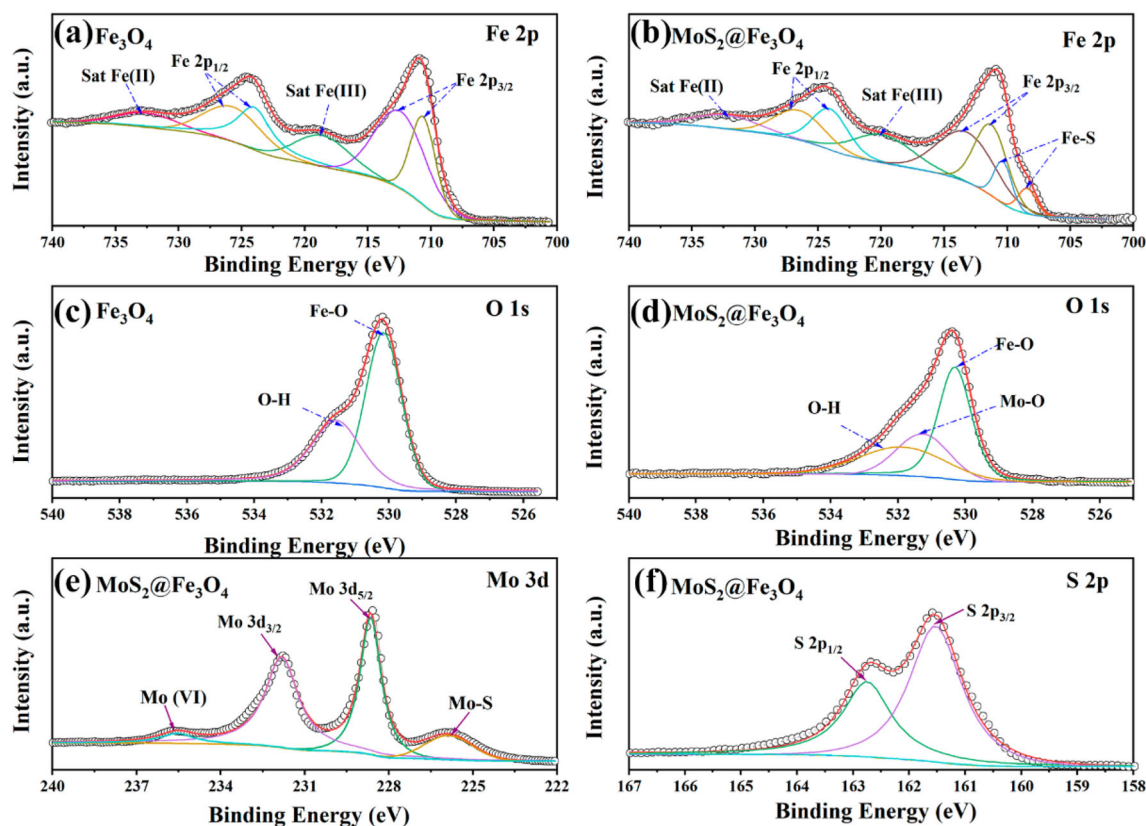


Fig. 3 X-ray photoelectron spectra of **a** Fe 2p (Fe_3O_4), **b** Fe 2p ($\text{MoS}_2@\text{Fe}_3\text{O}_4$), **c** O 1s (Fe_3O_4), **d** O 1s ($\text{MoS}_2@\text{Fe}_3\text{O}_4$), **e** Mo 3d, and **f** S 2p in $\text{MoS}_2@\text{Fe}_3\text{O}_4$

and out-of-plane A_{1g} vibrational modes of MoS_2 , which were consistent with previous reports [35]. Relative to those for MoS_2 , both the $E_1 2g$ and A_{1g} modes of $\text{MoS}_2@\text{Fe}_3\text{O}_4$ NFs shifted to lower energies (377.1 cm^{-1} and 403.3 cm^{-1} , respectively). The shift was attributed to the interaction of MoS_2 with Fe_3O_4 NPs that formed Fe–S bonds observed in the XPS [36]. This changed the stress in the MoS_2 lattice, which was affected by its multilayer structure, and eventually led to the change in the lattice vibrational frequency [37].

Figure 4b plots the magnetization curves for Fe_3O_4 NPs and $\text{MoS}_2@\text{Fe}_3\text{O}_4$ NFs. Both materials exhibited no significant coercivity or remanence, which verified the superparamagnetic property of the composites. The saturation magnetization of Fe_3O_4 NPs was approximately 59.3 emu/g , while that of $\text{MoS}_2@\text{Fe}_3\text{O}_4$ NFs was 24.5 emu/g . Hence, the introduction of the non-magnetic MoS_2 NF component decreased the magnetization. Photographs of magnetic enrichment

are illustrated in the inset of Fig. 4b. Because the NFs were superparamagnetic, the nanoflowers could be redistributed by slight shaking after the external magnetic field was removed, which enabled rapid biological detection.

3.2 Rapid and ultra-sensitive detection via $\text{MoS}_2@\text{Fe}_3\text{O}_4$ NF Raman probes

The biological detection of the dual-functional $\text{MoS}_2@\text{Fe}_3\text{O}_4$ NFs was evaluated utilizing the MoS_2 Raman peaks as probe signals and human IgG as the antigen. The detection results using strategy I are shown in Fig. 5a. The RRS intensity decreased with decreasing concentration of the analyte (1 nM, 100 pM, 1 pM, and 100 fM). The weak RRS signal from MoS_2 was observed when the analyte concentration was 100 fM, but was almost invisible when the concentration was 10 fM. Therefore, the experimental detection limit using strategy I was 100 fM. The opportunity of coupling between the Raman probe

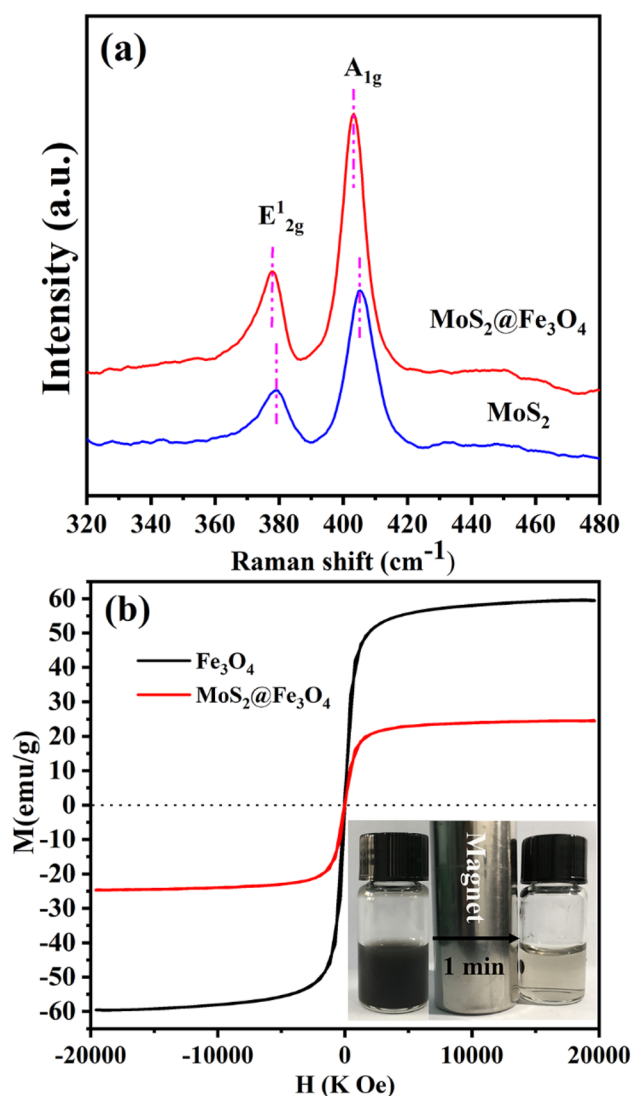


Fig. 4 **a** Raman spectra of MoS₂ and MoS₂@Fe₃O₄ nanoflowers (NFs). **b** Magnetization curves of Fe₃O₄ nanoparticles and MoS₂@Fe₃O₄ NFs. Inset: photographs showing magnetic separation

and the Au substrate was enhanced by shaking. However, that was insufficient for detecting very low concentrations. In strategy II, the immunological substrate immersed in the probe solution was placed above a commercial magnet (~ 1.2 T). The “antibody-analyte-antibody” sandwich structure was a bridge between the RRS of MoS₂ and the Au substrate. The detection results are shown in Fig. 5b. The

RRS signal of the 0.01 fM analyte was negligible, but that for the 0.1 fM analyte was strong. Hence, the detection limit for strategy II was enhanced by three orders-of-magnitude relative to that for strategy I, and was also better than previous reports [38, 39]. Standard deviations of the Raman peak intensities are shown in Fig. 5a, b. To verify the detection specificity, RRS measurements were performed in the absence of the analyte (“blank” in Fig. 5). No MoS₂ fingerprint Raman signal was obtained, indicating that non-specific adsorption did not occur between the Raman probe and the Au substrate.

Another benefit of the magnetic RRS immunoassay was that the detection time was significantly shortened. Because of the magnetic enrichment of the probe, the binding between the capture antibody (goat anti-human IgG on the substrate) and the analyte (human IgG coupled to the probe) was accelerated in a magnetic field during incubation. In strategy I, at least 1.5 h incubation was needed to obtain strong Raman signals (Fig. 5c). However, when a magnet was used to perform the assays (the concentration of the analytes was 100 pM), strong RRS signals were detected after 30 s of incubation, and the signal intensity was stable after 1 min (Fig. 5d). The results thus demonstrated that the Fe₃O₄ enhanced the detection limit and shortened the detection time.

4 Conclusions

In summary, magnetic MoS₂@Fe₃O₄ NF nanocomposites were fabricated. XPS characterization verified that the composites were covalently bonded. A magnetic-assisted rapid RRS detection method based on MoS₂@Fe₃O₄ NFs shortened detection times from 1.5 h to 1 min, and the detection limit was enhanced by three orders-of-magnitude (from 100 fM to 0.1 fM). The sandwich biosensor exhibited high specificity for human IgG. In addition, the MoS₂@Fe₃O₄ NF-based immunoassay was robust in various pH solutions and chemically stable. The rapid and ultra-sensitive antibody assay should also be applicable to viruses and early diagnoses of diseases such as cancer.

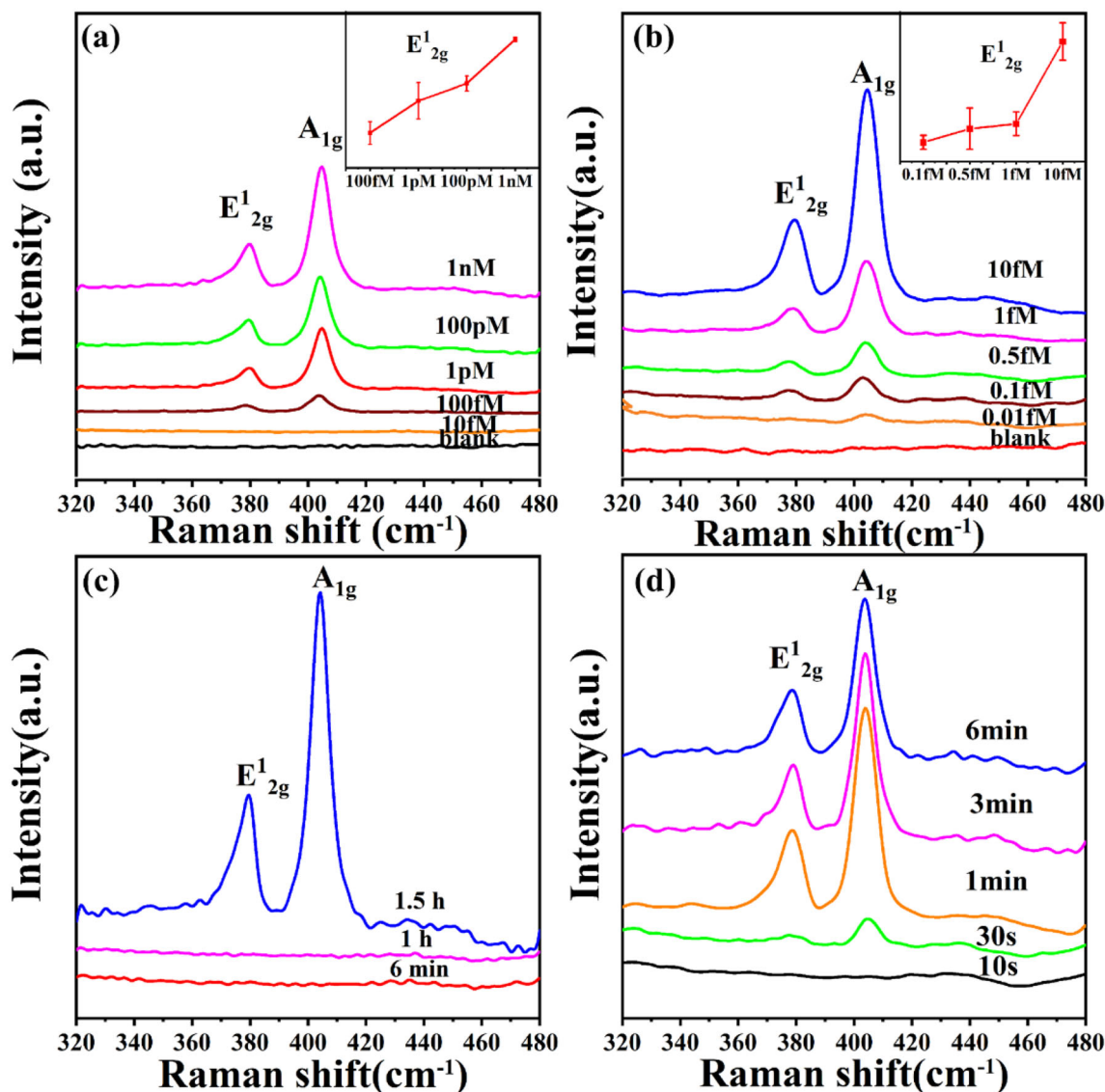


Fig. 5 Raman spectra of the immunoassays: **a**, **b** various concentrations of analyte; **c**, **d** various incubation times. **a** and **c** correspond to strategy I (without magnetic field), **b** and

d correspond to strategy II (1.2-T magnetic field, 100 pM). The insets are error analysis plots of the E1 2 g mode intensity

Acknowledgements

This work was supported by the “111” Project of China (D17017), the Developing Project of Science and Technology of Jilin Province (202002040JC, 20200201266JC, 20200201271JC), the International Science and Technology Cooperation Project of Jilin province (20190701029GH) and the Project of Education Department of Jilin Province (JJKH20200730KJ). We thank Liwen Bianji (Edanz) (www.liwenbianji.cn) for editing the language of a draft of this manuscript.

Author contributions

TZ contributed toward writing original draft, investigation, data curation, and formal analysis. XC contributed toward conceptualization, manuscript writing, reviewing, and editing, methodology, visualization, project administration, and funding acquisition. FJ contributed toward investigation, manuscript writing, reviewing, and editing, funding acquisition. MX contributed toward manuscript writing, reviewing, and editing, and funding acquisition. YZ collected resources, and contributed toward manuscript writing, reviewing, and editing,

and funding acquisition. JL contributed toward conceptualization, supervision, manuscript writing, reviewing, and editing, and funding acquisition.

Data Availability

The datasets are available from the corresponding author upon reasonable request.

Declarations

Conflict of interest Authors declare no conflicts of interest.

Ethical approval The authors declare that all data in this paper are original and have not been published in any other journal. This paper did not involve unethical treatment of animals.

Consent for participate All authors have provided consent to participate.

Consent for publication All authors have read the manuscript provided for publication.

References

- J Li J Wang X Zhang H Chang W Wei 2018 *Sensors and Actuators B: Chemical* 273 1300 <https://doi.org/10.1016/j.snb.2018.07.046>
- X Wang S-C Huang S Hu S Yan B Ren 2020 *Nature Reviews Physics* 2 253 <https://doi.org/10.1038/s42254-020-0171-y>
- MK Masud J Na M Younus 2019 *Chem Soc Rev* 48 5717 <https://doi.org/10.1039/c9cs00174c>
- Y Pang J Shi X Yang C Wang Z Sun R Xiao 2020 *Biosens Bioelectron* 148 111800 <https://doi.org/10.1016/j.bios.2019.111800>
- X Li J Wei KE Aifantis 2016 *J Biomed Mater Res A* 104 1285 <https://doi.org/10.1002/jbm.a.35654>
- V Kumar D Kukkar B Hashemi K-H Kim A Deep 2019 *Advanced Functional Materials* <https://doi.org/10.1002/adfm.201807859>
- K Wu D Su J Liu R Saha JP Wang 2019 *Nanotechnology* 30 502003 <https://doi.org/10.1088/1361-6528/ab4241>
- S Jamil MRSA Janjua 2017 *J. Cluster Sci.* 28 2369 <https://doi.org/10.1007/s10876-017-1256-3>
- H Shao H Lin Z Guo 2019 *Biosens Bioelectron* 143 111616 <https://doi.org/10.1016/j.bios.2019.111616>
- Z Chaloupkova A Balzerova J Barinkova 2018 *Anal Chim Acta* 997 44 <https://doi.org/10.1016/j.aca.2017.10.008>
- S Kang A Rahman E Boeding PJ Vikesland 2020 *Analyst* 145 4358 <https://doi.org/10.1039/d0an00711k>
- Y Pang N Wan L Shi 2019 *Anal Chim Acta* 1077 288 <https://doi.org/10.1016/j.aca.2019.05.059>
- WE Hong IL Hsu SY Huang 2018 *J. Mater. Chem. B* 6 5689 <https://doi.org/10.1039/c8tb00599k>
- T Zhou M Fan R You 2020 *Anal. Chim. Acta* 1104 199 <https://doi.org/10.1016/j.aca.2020.01.017>
- Y Li J Heo CK Lim 2015 *Biomaterials* 53 25 <https://doi.org/10.1016/j.biomaterials.2015.02.056>
- Y Zhou CH Liu Y Sun 2012 *J. Biomed. Opt.* 17 116021 <https://doi.org/10.1117/1.JBO.17.11.116021>
- M Harz CL Bockmeyer P Rösch RA Claus J Popp 2007 *Med. Laser Appl.* 22 87 <https://doi.org/10.1016/j.mla.2007.06.001>
- X Hong X Chu P Zou Y Liu G Yang 2010 *Biosens Bioelectron* 26 918 <https://doi.org/10.1016/j.bios.2010.06.066>
- F Li Y Li J Feng 2018 *Biosens Bioelectron* 100 512 <https://doi.org/10.1016/j.bios.2017.09.048>
- SS Singha S Mondal TS Bhattacharya 2018 *Biosens Bioelectron* 119 10 <https://doi.org/10.1016/j.bios.2018.07.061>
- J Jiang Q Shen P Xue 2020 *Chem. Select* 5 354 <https://doi.org/10.1002/slct.201903924>
- M Tong F Liu Q Dong Z Ma W Liu 2020 *J. Hazard Mater* 385 121604 <https://doi.org/10.1016/j.jhazmat.2019.121604>
- T Lin J Wang L Guo F Fu 2015 *J. Phys. Chem. C* 119 13658 <https://doi.org/10.1021/acs.jpcc.5b02516>
- L Wang F Liu A Pal 2021 *Carbon* 179 327 <https://doi.org/10.1016/j.carbon.2021.04.024>
- H Wu Z Qiu 2021 *J. Alloys Comp* <https://doi.org/10.1016/j.jallcom.2021.160264>
- X Zhang Y Dong F Pan Z Xiang X Zhu W Lu 2021 *Carbon* 177 332 <https://doi.org/10.1016/j.carbon.2021.02.092>
- J Su H Hao X Lv X Jin Q Yang 2020 *Colloids Surf. A* <https://doi.org/10.1016/j.colsurfa.2020.124751>
- Q Hong C Liu Z Wang 2021 *Chem. Eng. J.* <https://doi.org/10.1016/j.cej.2021.129238>
- N Zhao H Fan M Zhang 2020 *Chem. Eng. J.* <https://doi.org/10.1016/j.cej.2020.124477>
- C Zhou Q Wang XH Yan 2020 *Ceramics Int.* 46 15385 <https://doi.org/10.1016/j.ceramint.2020.03.083>
- MA Baker R Gilmore C Lenardi W Gissler 1999 *Appl. Surf. Sci.* 150 255 [https://doi.org/10.1016/S0169-4332\(99\)00253-6](https://doi.org/10.1016/S0169-4332(99)00253-6)
- D Mu Z Chen H Shi N Tan 2018 *RSC Adv.* 8 36625 <https://doi.org/10.1039/c8ra06537c>
- J Kibsgaard Z Chen BN Reinecke TF Jaramillo 2012 *Nat. Mater.* 11 963 <https://doi.org/10.1038/nmat3439>
- Z Wang J Zhang T Wen 2020 *Sci Total Environ* 699 134341 <https://doi.org/10.1016/j.scitotenv.2019.134341>
- HS Matte A Gomathi AK Manna 2010 *Angew Chem Int Ed Engl* 49 4059 <https://doi.org/10.1002/anie.201000009>

36. Z Zhang R Shi F Wang 2020 J. Mater. Sci. 56 5015 <https://doi.org/10.1007/s10853-020-05588-1>
37. J Yu W Yin X Zheng 2015 Theranostics 5 931 <https://doi.org/10.7150/thno.11802>
38. Y Liu H Wang S Li 2018 Sensors and Actuators B: Chemical 258 402 <https://doi.org/10.1016/j.snb.2017.11.083>
39. A Kenry Geldert X Zhang H Zhang CT Lim 2016 ACS Sensors 1 1315 <https://doi.org/10.1021/acssensors.6b00449>

Publisher's Note Springer Nature remains neutral with regard to jurisdictional claims in published maps and institutional affiliations.